Journal of Applied Fluid Mechanics, Vol. 10, No. 4, pp. 1029-1043, 2017.
Available online at www.jafmonline.net, ISSN 1735-3572, EISSN 1735-3645.
DOI: 10.18869/acadpub.jafm.73.241.26311

Computation of Developing Turbulent Flow through a Straight Asymmetric Diffuser with Moderate Adverse Pressure Gradient

S. Salehi[1†], M. Raisee[1] and M. J. Cervantes[2,3]

[1] *Hydraulic Machinery Research Institute, School of Mechanical Engineering, College of Engineering, University of Tehran, Tehran, 11155/4563, Iran*
[2] *Division of Fluid and Experimental Mechanics, Luleå University of Technology, Luleå, 97187, Sweden*
[3] *Water Power Laboratory, Norwegian University of Science and Technology, Trondheim, 7491, Norway*

†*Corresponding Author Email: s.salehi@ut.ac.ir*

(Received March 15, 2016; accepted March 6, 2017)

ABSTRACT

In this paper, numerical investigation of three-dimensional, developing turbulent flow, subjected to a moderate adverse pressure gradient, has been investigated using various turbulence models, namely: the low-Re $k-\varepsilon$, the SST $k-\omega$, the v^2-f and a variant of Reynolds stress model. The results are compared with the detailed velocity and pressure measurements. Since the inlet condition is uncertain, a study was first performed to investigate the sensitivity of the results to the inlet boundary condition. The results showed the importance of including the contraction effects. It is seen that the developing flow inside the straight duct, is highly sensitive to the inlet boundary condition. The comparisons indicate that all turbulence models are able to predict a correct trend for the centerline velocity and pressure recovery inside the straight duct and diffuser but the low-Re $k-\varepsilon$ and RSM turbulence models yield more realistic results. The SST $k-\omega$ model largely overpredicts the centerline velocity and boundary layer thickness in the straight duct. The comparisons of the numerical results also revealed that the RSM model, due to its anisotropic formulation, is able to reproduce the secondary flows. As expected, the RSM model demonstrates the best performance in prediction of the flow field and pressure recovery in the asymmetric diffuser.

Keywords: Moderate adverse pressure gradient; Asymmetric diffuser; Turbulent developing flow; Computational fluid dynamics; RANS models.

1. INTRODUCTION

Developing turbulent flow under adverse pressure gradient (APG) occurs in various fluid flow related engineering applications. Turbulent flow around aircrafts, automobiles and inside the draft tube of hydraulic turbines, are a few examples of such applications. Hence, accurate prediction of turbulent flow under adverse pressure gradient can contribute in the optimization of fluid machineries. Indeed, the presence of APG can greatly affect the performance and efficiency of hydraulic machines. If a turbulent boundary layer flow encounters a large APG, flow becomes unstable and if the APG is sufficiently large, flow separates from the wall and forms a recirculating region. Such recirculation region often has negative consequences such as: increase in the pressure drag, decrease in lift and increase in head losses. More specifically, flow separation could also have destructive effects on performance of hydraulic machinery equipment such as draft tube where the pressure recovery is restricted by attachment of flow to the walls.

Turbulent flow under APG has been the subject of a large number of experimental and numerical investigations. Among all the previous studies, the experimental investigations conducted by Clauser (1954) and Bradshaw (1967) can be considered as the first studies on this topic. Both studies measured characteristics of equilibrium turbulent boundary layers where the pressure gradient parameter is kept constant. Nagano *et al.* (1993) experimentally studied the behavior of turbulent boundary layer under moderate and strong adverse pressure gradients. They showed that with increase in adverse pressure gradients, the near wall velocity profile shifts below the standard log-law, indicating a reduction in the viscous sub-layer thickness.

Furthermore, the presence of an APG could significantly affect the distributions of turbulence quantities. Rai (1986) conducted experiments in a wind tunnel for three arbitrary adverse pressure gradient flows. The experimental observations clearly indicate that wall-wakes in adverse pressure gradient can be adequately described by the two-layer model proposed.

Direct numerical simulation (DNS) has been employed by Lee and Sung (2008) to investigate the effects of an adverse pressure gradient on a turbulent boundary layer. Their numerical results showed that the mean flow quantities are greatly affected by an APG, and the coherent structures in the outer layer of the APG flows were more activated than those in the zero pressure gradient flows. This was attributed to increased turbulence intensities, shear stresses and pressure fluctuations in the APG systems. More recently, Inouea *et al.* (2013) reported large eddy simulation (LES) of a turbulent boundary layer at high Reynolds number subject to an adverse pressure gradient. The stretched-vortex model (Chung and Pullin, 2009) was used for the subgrid-scale modeling. The results showed self-similarity in the velocity statistics over a wide range of Reynolds numbers. It was concluded that the boundary layers under adverse pressure gradient are far from an equilibrium state.

Among numerous applications of adverse pressure gradient flows, diffusers are one of the most commonly used flow devices in the industry, especially in hydraulic machines. Therefore, investigation of turbulent flow through diffusers has been an important research topic for fluid mechanics researchers. In the following, some of the investigations related to turbulent flow through diffusers will be reviewed.

Obi *et al*. (1993) performed laser Doppler anemometry (LDA) measurements in an asymmetric diffuser with an expansion ratio of 4.7, a single deflection of 10^{o} and a turbulent fully developed inlet condition. Buice and Eaton (1996) argued that the experimental data from Obi *et al*. (1993) had several deficiencies when comparing with their numerical results. The most noticeable problem was that the experimental data of Obi *et al*. (1993) did not appear to satisfy the mass conservation. Hence, they performed new detailed measurements in the reproduction of the Obi experiments using hot-wire and pulsed-wire measurements. The experimental works by Obi *et al*. (1993) and Buice and Eaton (1996) have received much attention because of the fully-developed inlet condition, presence of flow separation and flow development downstream of the reattachment point. For example, Kaltenback *et al*. (1999) conducted a numerical investigation on Obi diffuser using LES. They showed that a detailed representation of the inflow velocity field is critical for accurate prediction of the flow inside the diffuser. They also found that the sub-grid scale model plays a major role for prediction of both mean momentum and turbulent kinetic energy. Schlüter *et al*. (2005) also conducted LES computations of Obi diffuser flow. They used three different mesh sizes and different modeling approaches to examine the influence of the mesh resolution and four subgrid models, namely: no model (implicit LES), the standard Smagorinsky model, the dynamic Smagorinsky model and the dynamic localization model. The mesh refinement study demonstrated improvement in the predictions. Among the subgrid strategies examined, the dynamic Smagorinsky model performed the best. Iaccarino (2001) used three commercial CFD codes, namely: CFX, Fluent, and Star-CD, and two turbulence models (the low-Re $k-\varepsilon$ and the v^2-f) for the numerical simulation of Obi diffuser. The numerical results showed that the v^2-f model produces more accurate results than the low-Re $k-\varepsilon$ model when comparisons were made with the experimental data and LES predictions. The $k-\varepsilon$ calculations do not show any recirculation region, while the v^2-f model reproduces the length of the separation bubble within 6 percent of the measured value. More recently, El-Behery and Hamed (2011) employed the commercial code Fluent to examine the capabilities of several turbulence models in prediction of turbulent flow in the planar asymmetric diffuser of Obi diffuser. The comparisons showed that the results of the v^2-f turbulence model agree best with the experimental data while the RSM model was shown to give unexpected poor results.

Cherry *et al*. (2008 and 2009) performed experiments to measure the mean velocity field in two separate 3D asymmetric diffusers using the magnetic resonance velocimetry method. The measured flow fields in both diffusers showed 3D boundary layer separation but the structure of the separation bubble exhibited a high degree of sensitivity to the diffuser geometrical dimensions. In their experiment, a fully-developed flow condition was established at the diffuser entry which is suitable for the turbulence modeling validation proposes. Similar to Obi diffuser, the Cherry diffuser has been used as a benchmark for the investigation of performance of turbulence models and numerical approaches in recent years. A direct numerical simulation of turbulent flow in the Cherry diffuser (Cherry *et al*., 2008) was conducted by Ohlsson *et al*. (2010) with a massively parallel high-order spectral element method and their results were in good agreement with the experimental data. Jakirlić *et al*. (2010) applied LES and a zonal hybrid LES/RANS scheme to predict the turbulent flow through the 3D diffuser investigated by Cherry *et al*. (2008). Both modeling strategies gave acceptable results for the time-averaged quantities. Jeyapaul (2011) also performed numerical simulations on Cherry diffuser using RANS models. The results showed that the linear eddy-viscosity models fail to predict separation on the correct wall of the 3D diffuser. However, the explicit algebraic RSM (EARSM) is able to predict separation accurately. The EARSM predicted

quantitatively the mean flow field, however the Reynolds stresses were incorrect and the wall pressure was under predicted.

Cervantes and Engström (2008) experimentally investigated the turbulent flow inside an asymmetric diffuser with a moderate adverse pressure gradient using LDA technique. The diffuser has a diverging upper wall, designed to yield an approximately constant adverse pressure gradient, which opens up from an angle of $2.5°$ at the beginning to $7.5°$ at the end. The diffuser is a generic model of the rectangular diffuser found at the end of most hydropower turbines of the Francis and Kaplan types with an elbow draft tube. The elbow draft tube is found immediately after the runner and, as shown in Fig. 1, composed of a conical diffuser, an elbow and a straight rectangular diffuser. Although the Reynolds number was small compared to full-scale turbines, the flow is still fully turbulent and the large viscous length-scale allows detailed measurements in the boundary layer up to $y^+ \approx 1$. They carried out measurements in steady regime and three different pulsating regimes based on the dimensionless frequency ($\omega^+ = \omega\nu / u_\tau^2$) namely: quasi-steady ($\omega^+ < 0.005$), relaxation ($0.005 < \omega^+ < 0.02$) and quasi-laminar ($0.02 < \omega^+ < 0.04$). This test case provides accurate experimental data for validating CFD calculations with focus on adverse pressure gradient effects and non-trivial boundary conditions: both important for hydropower simulations.

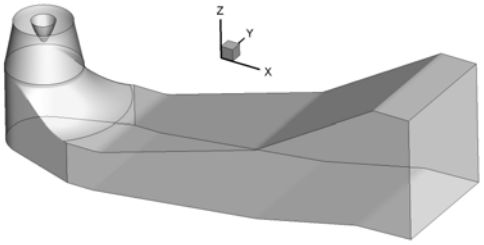

Fig. 1. Schematic of a draft tube.

In the present study, numerical investigations are performed on the diffuser studied experimentally by Cervantes and Engström in statistically stationary condition. The main objective of the present study is to examine the effectiveness of various turbulence models in prediction of developing turbulent flow subjected to the adverse pressure gradient. To the best of our knowledge authors, the present paper is the first attempt to investigate the 3D asymmetric diffusers with the developing inflow condition using different turbulence models.

2. PROBLEM DESCRIPTION

The geometry investigated in this paper has been studied experimentally by Cervantes and Engström (2008). A schematic of the experimental setup used for their measurements is shown in the Fig. 2. A 2.102 *m* straight rectangular duct with a rectangular cross section of 0.1×0.15 m^2 is used upstream the diffuser. The flow is still developing at the end of the straight duct as found in hydropower systems. The hydraulic diameter of the straight duct calculated by $4A_{\text{duct}} / p$ is $D_h = 0.12$ m. Hence, the duct length is $17.5\, D_h$. The Reynolds number based on the bulk velocity and duct hydraulic diameter is 2×10^4 (flow rate of 2.47×10^{-3} m^3/s). A contraction (9:1) precedes the duct. In addition, the flow is tripped at the exit of the contraction by 2 mm plates, extruding 9.2 mm from the walls, corresponding to about 18% of the duct height and 12% of the duct width. The tripping was necessary to achieve repeatable conditions in the test section, as also found by Durst *et al.* (1998). Following the duct is an asymmetric diffuser with a diverging upper wall designed to yield an approximately constant adverse pressure gradient. The main part of this experimental setup, from the duct inlet to the diffuser outlet, is numerically modeled here. Fig 3(a) shows a 3D view of the geometry. In addition, Fig. 3(b) represents a 2D schematic of the diffuser with the variation of the diffuser angle. The diffuser opens up to a cross section of 0.15×0.15 m^2 at the outlet (x= 2.772 m). The diffuser angle increases from $2.5°$ at the beginning to $7.5°$ at x= 2.772 m. The flow field inside the diffuser has been investigated at three stations, namely: x=2.082 m, 2.357 m and 2.632 m. As shown in Fig 3. (b), the first station is 20 mm before the start of the diffuser and the second and third stations are at about 40% and 80% of the diffuser length downstream, respectively.

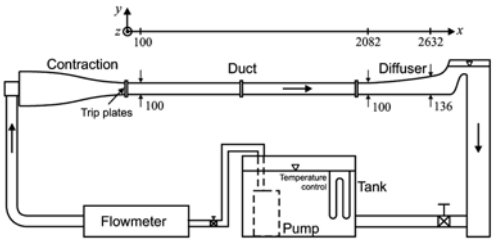

Fig. 2. Experimental setup used by Cervantes and Engström (2008) (dimensions in mm).

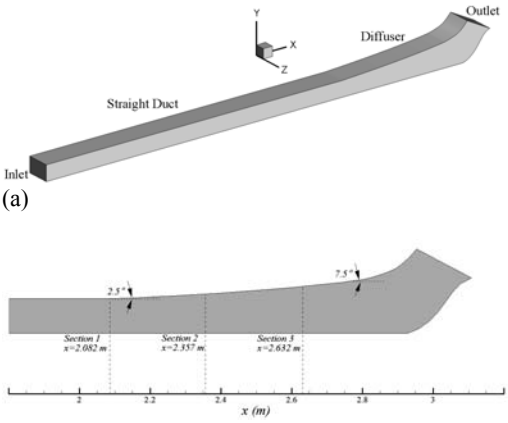

Fig. 3. (a) 3D l view of the domain. (b) 2D Schematic of examined diffuser.

3. MATHEMATICAL FORMULATION

3.1 Mean Flow Equations

For an incompressible turbulent flow, the time averaged equations of continuity and momentum are written as:

$$\frac{\partial U_j}{\partial x_j} = 0 \tag{1}$$

$$\frac{\partial (U_i U_j)}{\partial x_j} = \frac{-1}{\rho}\frac{\partial P}{\partial x_i} + \frac{\partial}{\partial x_j}\left(\nu \frac{\partial U_i}{\partial x_j} - \overline{u_i u_j}\right) \tag{2}$$

where ρ and ν are fluid density and kinematic viscosity and $-\rho\overline{u_i u_j}$ represents the Reynolds stress tensor.

3.2 Turbulence Modeling Equations

The turbulence models employed for computations are the low-Re $k-\varepsilon$ model (proposed by Launder and Sharma, 1974), the SST $k-\omega$ model (Menter, 1994), the v^2-f model (Durbin, 1995) and a variant of Reynolds stress model (Gibson and Launder, 1978).

3.3.1 Low-Re $k-\varepsilon$ Model

In this turbulence model, the unknown Reynolds stresses are obtained from the Boussinesq hypothesis:

$$\overline{u_i u_j} = -\nu_t\left(\frac{\partial U_i}{\partial x_j} + \frac{\partial U_j}{\partial x_j}\right) + \frac{2}{3}k\delta_{ij} \tag{3}$$

where the turbulent viscosity is calculated via:

$$\nu_t = c_\mu f_\mu \frac{k^2}{\varepsilon} \tag{4}$$

To obtain ν_t, transport equations for the turbulence kinetic energy, k and its dissipation rate are solved. The transport equation for the turbulent kinetic energy is written as:

$$\frac{\partial}{\partial x_j}(U_j k) = \frac{\partial}{\partial x_j}\left[\left(\nu + \frac{\nu_t}{\sigma_k}\right)\frac{\partial k}{\partial x_j}\right] + P_k - \tilde{\varepsilon} - 2\nu\left(\frac{\partial \sqrt{k}}{\partial x_j}\right)^2 \tag{5}$$

where P_k, the generation rate of turbulent kinetic energy, is obtained from:

$$P_k = -\overline{u_i u_j}\frac{\partial U_i}{\partial x_j} \tag{6}$$

The homogeneous dissipation rate of turbulent kinetic energy, $\tilde{\varepsilon}$, is obtained by solving the following equation:

$$\frac{\partial}{\partial x_j}(U_j \tilde{\varepsilon}) = \frac{\partial}{\partial x_j}\left[\left(\nu + \frac{\nu_t}{\sigma_\varepsilon}\right)\frac{\partial \tilde{\varepsilon}}{\partial x_j}\right] + c_{\varepsilon 1}\frac{\tilde{\varepsilon}}{\sigma_\varepsilon}P_k - c_{\varepsilon 2}f_2\frac{\tilde{\varepsilon}^2}{k} + E \tag{7}$$

The empirical constants of the model are presented in Table 1.

The homogeneous dissipation rate can be related to the true dissipation rate through:

$$\tilde{\varepsilon} = \varepsilon - 2\nu\left(\frac{\partial \sqrt{k}}{\partial x_j}\right) \tag{8}$$

The damping functions f_μ and f_2 are given by:

$$f_\mu = \exp\left[-3.4/(1+0.02\tilde{R}_t)^2\right]$$
$$f_2 = 1 - 0.3\exp(-\tilde{R}_t^2) \tag{9}$$

where $\tilde{R}_t = k^2/\nu\tilde{\varepsilon}$ is the local turbulent Reynolds number.

The term E is first introduced by Jones and Launder (1972) and is expressed as:

$$E = 2\nu\nu_t\left(\frac{\partial^2 U_i}{\partial x_j \partial x_k}\right)^2 \tag{10}$$

Table 1 Empirical constant of linear $k-\varepsilon$ model

c_μ	$c_{\varepsilon 1}$	$c_{\varepsilon 2}$	σ_k	σ_ε
0.09	1.44	1.92	1.0	1.3

3.3.2. SST $k-\omega$ Model

The main idea of the SST $k-\omega$ model is to combine the robustness of the $k-\omega$ turbulence model near walls with the capabilities of the $k-\varepsilon$ model away from the walls. The model uses the Boussinesq hypothesis (equation (3)) to obtain the Reynolds stresses. The turbulent viscosity is calculated via:

$$\nu_t = \frac{a_1 k}{\max(a_1\omega, SF_2)} \tag{11}$$

where k and ω are obtained by solving the following transport equations:

$$\frac{\partial}{\partial x_j}(U_j k) = \frac{\partial}{\partial x_j}\left[\left(\nu + \sigma_k\nu_t\right)\frac{\partial k}{\partial x_j}\right] + \tilde{P}_k - \beta^* k\omega \tag{12}$$

$$\frac{\partial}{\partial x_j}(U_j \omega) = \frac{\partial}{\partial x_j}\left[\left(\nu + \sigma_\omega\nu_t\right)\frac{\partial \omega}{\partial x_j}\right] + \alpha S^2 - \beta\omega^2 + 2(1-F_1)\sigma_{\omega 2}\frac{1}{\omega}\frac{\partial k}{\partial x_j}\frac{\partial \omega}{\partial x_j} \tag{13}$$

The blending function F_1 is defined by:

$$F_1 = \tanh\left\{\left\{\min\left[\max\left(\frac{\sqrt{k}}{\beta^* \omega y}, \frac{500\nu}{y^2\omega}\right), \frac{4\rho\sigma_{\omega 2}k}{CD_{k\omega}y^2}\right]\right\}^4\right\} \quad (14)$$

where $CD_{k\omega} = \max\left(2\rho\sigma_{\omega 2}\frac{1}{\omega}\frac{\partial k}{\partial x_j}\frac{\partial \omega}{\partial x_j}, 10^{-10}\right)$ and y is the distance to the nearest wall.

The blending function F_1 is zero away from surfaces ($k-\varepsilon$ model) and switches to one inside the boundary layer ($k-\omega$ model). The ***S*** term in the turbulent viscosity expression is the invariant strain rate and the second blending function F_2 is defined by:

$$F_2 = \tanh\left\{\left[\max\left(\frac{2\sqrt{k}}{\beta^* \omega y}, \frac{500\nu}{y^2\omega}\right)\right]^2\right\} \quad (15)$$

The production term has a limiter to prevent the build-up of unrealistic high turbulence energy in the stagnation regions:

$$\tilde{P}_k = \min\left(P_k, 10\beta^* \rho k\omega\right) \quad (16)$$

All constants are computed by a blend from the corresponding constants of the $k-\varepsilon$ and the $k-\omega$ model via $\alpha = \alpha_1 F_1 + \alpha_2(1-F_1)$. The constants of the SST model are given in Table 2.

Table 2 Empirical constant of $k-\omega$ model

σ_{k1}	0.85
σ_{k2}	1.0
$\sigma_{\omega 1}$	0.5
$\sigma_{\omega 2}$	0.856
β^*	0.09
β_1	3/40
β_2	0.0828
α_1	5/9
α_2	0.44

3.3.3 $v^2 - f$ Model

The $v^2 - f$ model (developed by Durbin, 1995) is similar to the standard $k-\varepsilon$ model. In addition, it incorporates some near-wall turbulence anisotropy as well as non-local pressure-strain effects. Instead of turbulent kinetic energy, k, the $v^2 - f$ model uses a velocity scale $\overline{v^2}$ (velocity fluctuation normal to the streamlines) for the evaluation of the eddy viscosity. The anisotropic wall effects are modeled through the elliptic relaxation function, f, by solving a separate elliptic equation of the Helmholtz type. The Boussinesq approximation is still used for the evaluation of the Reynolds stresses. The eddy viscosity ν_t is given by:

$$\nu_t = c_\mu \overline{v^2} T \quad (17)$$

where the turbulent time-scale T and the turbulent length-scale L are obtained from the following expressions:

$$T = \max\left(\frac{k}{\varepsilon}, 6\sqrt{\frac{\nu}{\varepsilon}}\right) \quad (18)$$

$$L = c_L \max\left[\frac{k^{3/2}}{\varepsilon}, c_\eta \frac{\nu^{3/4}}{\varepsilon^{1/4}}\right] \quad (19)$$

The $\overline{v^2}$ transport equation is expressed as:

$$\frac{\partial}{\partial x_j}(U_j \overline{v^2}) = \frac{\partial}{\partial x_j}\left[\left(\nu + \frac{\nu_t}{\sigma_{\overline{v^2}}}\right)\frac{\partial \overline{v^2}}{\partial x_j}\right] + kf - \overline{v^2}\frac{\varepsilon}{k} \quad (20)$$

An elliptic equation is solved for the relaxation function f:

$$L^2 \frac{\partial^2 f}{\partial x_j^2} - f = \frac{1}{T}(c_1 - 1)\left(\frac{\overline{v^2}}{k} - \frac{2}{3}\right) - c_2 \frac{P_k}{\varepsilon} \quad (21)$$

The coefficients of $v^2 - f$ turbulence model are given in Table 3.

Table 3 Coefficients of $v^2 - f$ model

c_μ	0.19
$\sigma_{\overline{v^2}}$	1.0
σ_ε	1.3
$c_{\varepsilon 1}$	$1.3 + 0.25/\left[1+\left(c_L d/2L\right)^2\right]^4$
$c_{\varepsilon 2}$	1.9
c_1	1.4
c_2	0.3
c_L	0.3
c_η	70

3.3.4 RSM Model

The Reynolds Stress Model (RSM) is the most detailed and elaborate RANS turbulence model. In contrast to isotropic Boussinesq hypothesis based models, which use algebraic expressions for the evaluation of Reynolds stresses, the RSM models solve a partial differential transport equation for each Reynolds stress component.

The exact form of the Reynolds stress transport equations, shown below, can be derived via a mathematical manipulation on momentum equation:

$$\underbrace{\frac{\partial(U_k\overline{u_iu_j})}{\partial x_k}}_{convection} = \underbrace{-\frac{\partial(\overline{u_ku_iu_j})}{\partial x_k} - \frac{1}{\rho}\left(\frac{\partial\overline{u_jp}}{x_i} + \frac{\partial\overline{u_ip}}{x_j}\right)}_{turbulent-diffusion} - \underbrace{\overline{u_iu_k}\frac{\partial U_j}{\partial x_k} - \overline{u_ju_k}\frac{\partial U_i}{\partial x_k}}_{production} + \underbrace{\overline{\frac{p}{\rho}\left(\frac{\partial u_j}{\partial x_i} + \frac{\partial u_i}{\partial x_j}\right)}}_{pressure-strain} + \underbrace{\nu\frac{\partial^2\overline{u_iu_j}}{\partial x_k\partial x_k}}_{viscous-diffusion} - \underbrace{2\nu\overline{\frac{\partial u_i}{\partial x_k}\frac{\partial u_j}{\partial x_k}}}_{viscous-dissipation} \tag{22}$$

Clearly the diffusion, the pressure strain and the viscous dissipation terms are not explicitly defined and need to be modeled. The turbulent diffusion term is modeled using (Gibson and Launder, 1978):

$$D_{T,ij} = \frac{\partial}{\partial x_k}\left(\frac{\nu_t}{\sigma_k}\frac{\partial\overline{u_i'u_j'}}{\partial x_k}\right) \tag{23}$$

Also the viscous dissipation term can be simply modeled through $\varepsilon_{ij} = (2/3)\delta_{ij}\varepsilon$.

Here the variant of RSM proposed by Gibson and Launder (1978) is employed where the pressure strain correlation (or redistribution term) is expressed as:

$$\phi_{ij} = \phi_{ij,1} + \phi_{ij,2} + \phi_{ij,w} \tag{24}$$

where

$$\phi_{ij,1} = -C_1\rho\frac{\varepsilon}{k}\left[\overline{u_i'u_j'} - \frac{2}{3}\delta_{ij}k\right] \tag{25}$$

$$\phi_{ij,2} = -C_2\left[\left(P_{ij} - C_{ij}\right) - \frac{2}{3}\delta_{ij}\left(P - C\right)\right] \tag{26}$$

$$\phi_{ij,w} = -C_1'\frac{\varepsilon}{k}\left(\overline{u_k'u_m'}n_kn_m\delta_{ij} - \frac{3}{2}\overline{u_i'u_k'}n_jn_k - \frac{3}{2}\overline{u_j'u_k'}n_in_k\right)\frac{C_l k^{3/2}}{\varepsilon d} + C_2'\left(\phi_{km,2}n_kn_m\delta_{ij} - \frac{3}{2}\phi_{ik,2}n_jn_k - \frac{3}{2}\phi_{jk,2}n_in_k\right)\frac{C_l k^{3/2}}{\varepsilon d} \tag{27}$$

The P_{ij} and C_{ij} terms are production and convection terms respectively (defined in equation (22)); also $P = (1/2)P_{kk}$ and $C = (1/2)C_{kk}$. The model coefficients are given in Table 4. Re_t and a_{ij} are turbulent Reynolds number and Reynolds-stress anisotropy tensor, respectively.

4. NUMERICAL ASPECTS

4.1 Solver

All equations are discretized using finite-volume methodology on a collocated grid system. The open source C++ CFD code OpenFOAM (2011) was used to perform the computations. The second order upwind differencing scheme was employed for discretization of the convective terms in all transport equations. Gradient and Laplacian terms were discretized using the central differencing scheme. The pressure field is linked to the velocity field through the SIMPLE pressure correction algorithm. The convergence criteria were set to 10^{-5} for all equations.

4.2 Boundary Conditions

Accurate representation of inlet boundary condition is critical for numerical results inside a diffuser (Kaltenback *et al*., 1999). Since the contraction geometry is not fully known and boundary conditions are not available from experimental data, simulations are performed from section x=100 mm which is placed right after the tripping part. At this section, the velocity field for the streamwise and normal components is available from experimental data. Fig. 4 shows six different vertical and spanwise locations where the velocity components were measured using the LDA technique.

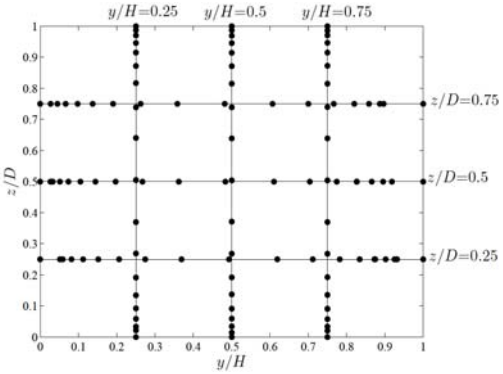

Fig. 4. The location of available experimental data at section x=100 mm.

Table 4 Coefficients of RSM model

C_μ	0.09
C_1	$1 + 2.58AA_2^{0.25}\left\{1 - \exp\left[-\left(0.0067\,\mathrm{Re}_t\right)^2\right]\right\}$
C_2	$0.75\sqrt{A}$
C_1'	$-2/3C_1 + 1.67$
C_2'	$\max\left[\left(2/3C_2 - 1/6\right)/C_2, 0\right]$
A	$\left[1 - 9/8\left(A_2 - A_3\right)\right]$
A_2	$a_{ik}a_{ki}$
A_3	$a_{ik}a_{kj}a_{ji}$
C_l	$C_\mu^{3/4}/\kappa$
κ	0.4187

A code was developed to evaluate the inlet boundary condition using a 3D surface fit on the experimental data with a polynomial interpolation scheme. Then, a moving average filter is applied on the interpolated data. The streamwise velocity is scaled by a factor to match the experimental flow

rate after integration. Finally, the velocity profiles are calculated on the cell centers at the inlet of the computational grid and are imposed as inlet boundary condition. The 3D surfaces obtained for both the streamwise and normal velocity components after smoothing are presented in Fig. 5. The spanwise component is obtained using the continuity equation assuming a negligible streamwise variation of u-velocity ($\partial u/\partial x \approx 0$), with respect to $\partial v/\partial y$ and $\partial w/\partial z$ because of the duct length. The experimental data for the streamwise velocity are not entirely symmetric. This may be induced by uncertainty in the contraction geometry and inflow condition.

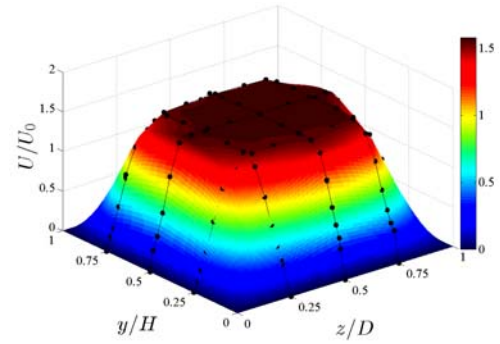

(a)

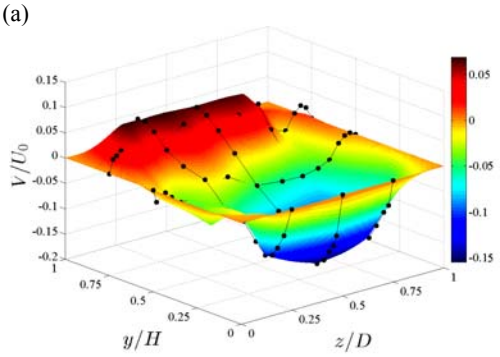

(b)

Fig. 5. 3D surfaces fitted to the experimental data. (a) streamwise and (b) normal velocity components.

Computations of the flow inside the described geometry are performed with uniform and non-uniform velocity boundary conditions to study their effects on the results. Figs. 6(a)-(c) illustrate the development of the mean streamwise velocity and fluctuating part of the streamwise and normal velocities along the centerline of the duct and diffuser for both inlet boundary conditions. It is observed that the numerical results of Case 1 (non-uniform inlet velocity) are significantly closer to the experimental data than those obtained in Case 2 (uniform). Hence, based on this comparison the first approach is used for the predictions presented in the following sections.

An isotropic turbulence field is assumed at the inlet of all cases due to the lack of experimental turbulent data at the inlet. The turbulent quantities at the inlet are calculated using turbulent intensity (I) and turbulent length-scale (l). Turbulent intensity is the ratio of velocity fluctuations to the mean velocity (U_0). Therefore, assuming an isotropic field, the turbulent kinetic energy is obtained by:

$$k = \frac{3}{2}(IU_0)^2 \tag{28}$$

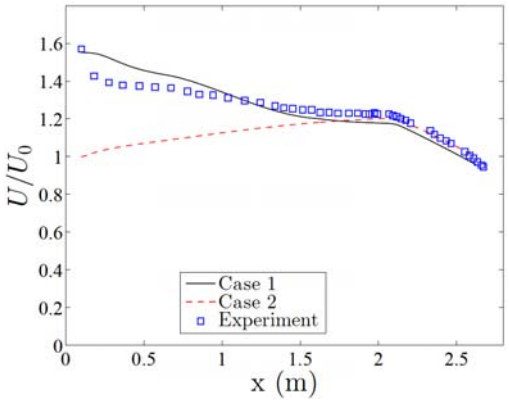

(a)

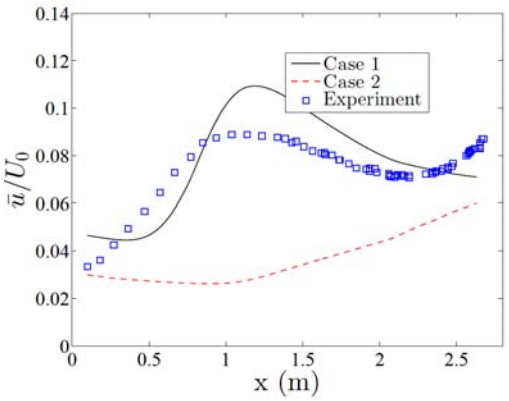

(b)

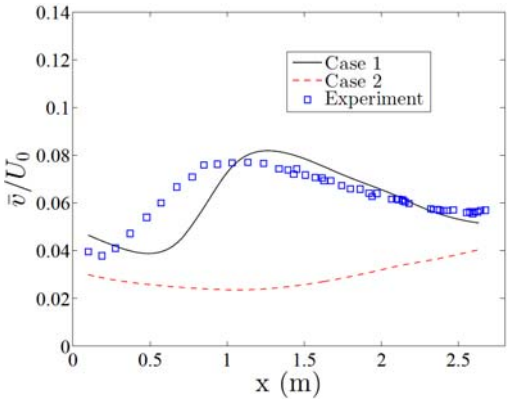

(c)

Fig. 6. Comparison between results of Case 1 (non-uniform inlet B.C.) and 2 (uniform inlet B.C.). (a) Mean streamwise velocity and fluctuating part of (b) streamwise and (c) normal velocities.

The homogeneous dissipation rate and specific dissipation rate are also obtained from:

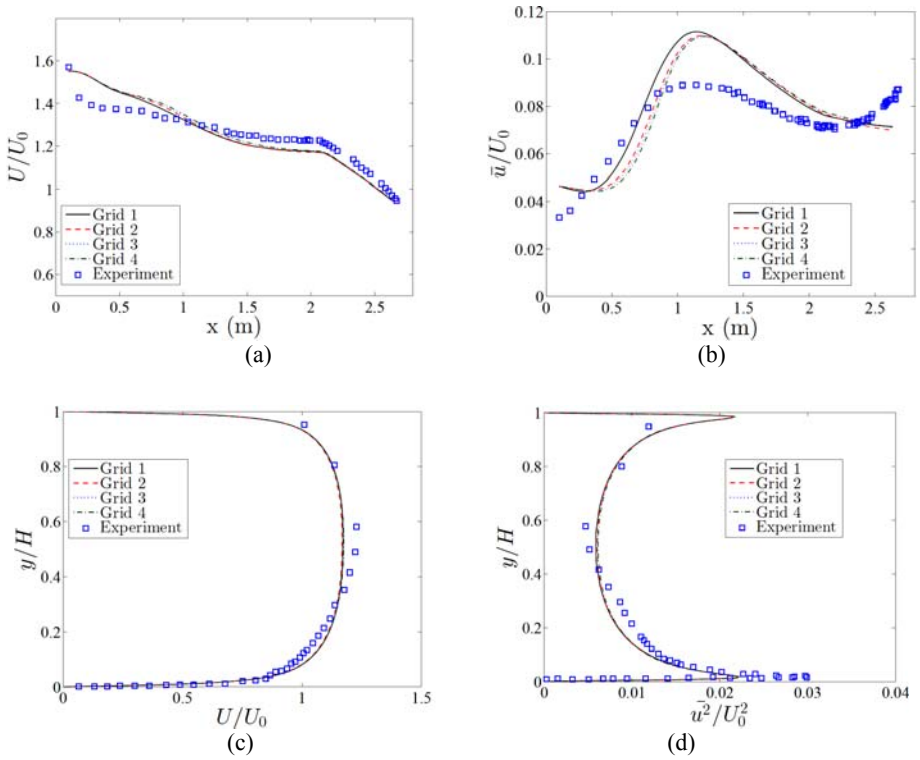

Fig.7. Results of the grid study; development of (a) mean streamwise velocity and (b) its fluctuations along the duct and diffuser centerline. Streamwise (c) velocity and (d) fluctuations profiles at (c) section *x*=2082 mm.

$$\tilde{\varepsilon} = \frac{c_\mu^{3/4} k^{3/2}}{l}, \quad \omega = \frac{k^{1/2}}{c_\mu^{1/4} l} \tag{29}$$

where l (turbulent length-scale) is set to $0.1D_h$. Hence, by choosing a turbulent intensity at the inlet, all other quantities can be calculated. Since there is no available experimental data on velocity fluctuations and turbulent intensity at the duct inlet, a study was performed on the effect of inlet turbulent intensity on the results of the mean flow and turbulent stresses in the straight duct and diffuser. The computations were performed using the RSM model and different turbulence intensities at the inlet and intensity of 3% was found to give accurate results. The pressure value at the inlet is computed using the zero-gradient condition normal to boundary. At the exit boundary, zero gradient boundary conditions along normal to the outlet were imposed for all variables (flow and turbulence) except pressure, which is considered as a constant value.

Since the models used in the present work are "low-Reynolds number" turbulence models, the near-wall region is resolved up to $y^+ \approx 1$. Hence, no special treatment (such as wall functions) is necessary for the wall boundary conditions of the mean flow and turbulence transport equations, i.e., the velocity components, turbulent kinetic energy, homogeneous dissipation rate, specific dissipation rate. In addition, for the RSM model, the wall boundary condition of velocity components, homogeneous dissipation rate and all components of Reynolds stress tensor are also set to zero. The pressure on wall is also obtained using the assumption of zero-gradient along normal to the wall.

4.3 Grid Study

To study the sensitivity of the computational results to the grid resolution, a grid study was performed using the RSM turbulence model. For this purpose, four different grids (from coarse grid of 470,000 cells to fine grid of 3,700,000 cells) have been generated. All of these grids are non-uniform and fully structured. As it was mentioned earlier all of turbulence models used in this investigation are "low-Reynolds number" and these grids are fine enough to resolve the near wall viscous sub-layer region. In addition, the grid points have been refined along the stream-wise direction around the diffuser because of high stream-wise gradients in these regions. Table 5 presents the specifications of the five computational grids generated for the grid study; n_x, n_y and n_z represent the number of nodes along stream-wise (x), normal (y) and cross-stream (z) directions, respectively.

The results obtained from the grid study for four different grids are presented in Fig. (7). The development of mean streamwise velocity and its corresponding fluctuation along the centerline of the duct and diffuser are illustrated in Fig. 7(a) and 7(b), respectively. Figs. 7(c) and 7(d) show

the variation of streamwise velocity and its fluctuation along a vertical line placed on the symmetry plane at section x=2082 mm. It can be noted from these four figures that although grid refinement slightly affects the velocity field inside the diffuser, it has more noticeable effects on the mean and fluctuating velocity in the developing region (straight duct). The results obtained on Grid 3 with 1.4×10^6 nodes are almost grid independent and a finer mesh would not give very different results. Thus, the subsequent computational results are obtained using Grid 3. Figs. 8(a) and 8(b) show the chosen grid in symmetry plane and inside the diffuser.

Table 5 Specifications of grids produced for the grid study

Grid No.	n_x	n_y	n_z	Distance from wall
Grid 1	156	45	68	$y^+ = O(1)$
Grid 2	213	52	78	$y^+ = O(1)$
Grid 3	265	60	90	$y^+ = O(1)$
Grid 4	390	80	120	$y^+ = O(1)$

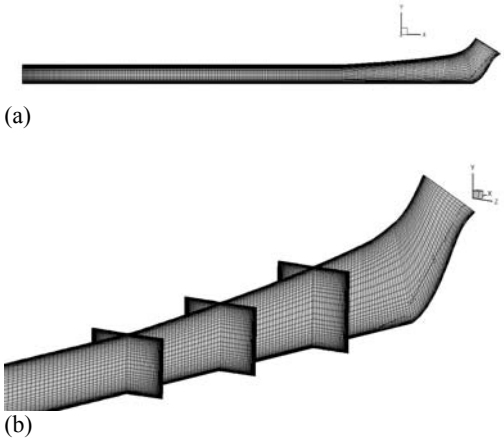

(a)

(b)

Fig. 8. Main grid used for the computations. Cells distribution on (a) Symmetry plane and (b) diffuser.

5. RESULTS AND DISCUSSION

In this section, the numerical results obtained using four turbulence models are presented and compared with the experimental data of Cervantes and Engström (2008).

The variation of the velocity along the centerline of the duct flows is generally sensitive to the development of the boundary layers in the duct. Non-tripped boundary layers will grow along the duct length, thereby forcing the bulk flow to accelerate along the centerline. However, in the present geometry, the flow is tripped right before the straight duct. With the current tripping, the bulk flow accelerates immediately and the shear layers induced by the tripping produce fast growing boundary layers.

Figure 9 shows the mean streamwise velocity (normalized with $U_0 = Q / A_{\text{duct}}$) along the centerline in the straight duct and the diffuser. In both the numerical and the experimental results, the streamwise velocity starts with an overshoot induced by the tripping and the sudden decrement of flow area. After the trip, velocity decreases, but the rate of velocity decrease reduces along the centerline due to the boundary layer growth. From x=1500 mm to the start of the diffuser, the velocity gradient becomes smaller, but flow does not show clear signs of reaching the fully-developed condition. As the flow enters the diffuser, the velocity drops rapidly due to the cross-sectional area increase. It is seen that all turbulence models have successfully predicted the general variation of the streamwise velocity along the centerline. There are significant differences between the results of these models. The SST $k-\omega$ model largely overpredicts the centerline streamwise velocity due to an overestimation of the boundary layer thickness. It is observed that the results of low-Re $k-\varepsilon$ and RSM turbulence models are closest to the experimental data both inside the straight duct and the diffuser.

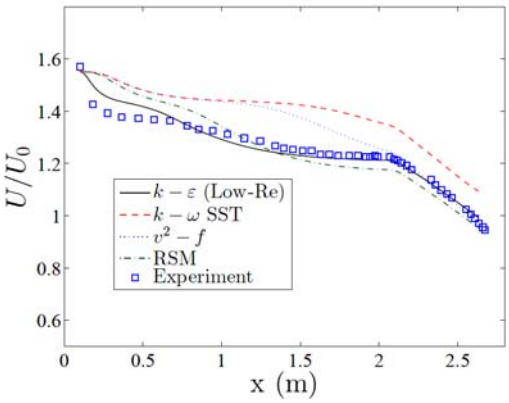

Fig. 9. Development of the streamwise velocity along centerline.

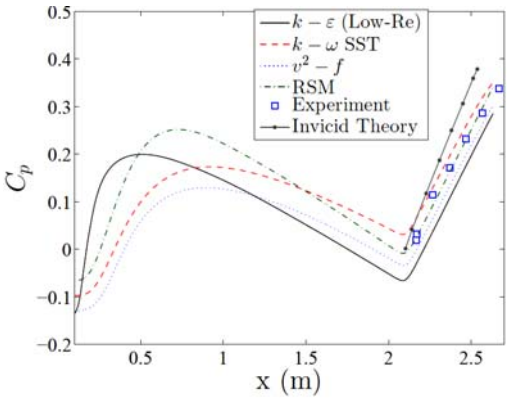

Fig. 10. Pressure coefficient distribution along the centerline of the upper wall.

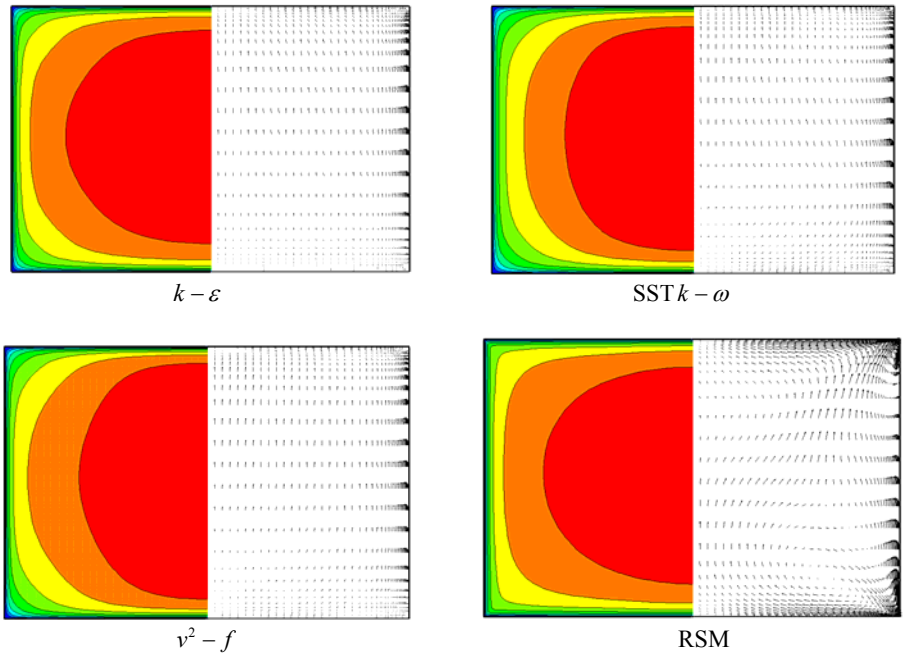

Fig. 11. Vectors of secondary flow (right) and Contours of streamwise velocity (left) in section *x*=2082 m.

The distribution of pressure coefficient, defined by:

$$C_p = \frac{p - p_{atm}}{\frac{1}{2}\rho U_0^2} \tag{30}$$

along the centreline of the upper wall is illustrated in Fig. 10. The pressure rises to a peak value and then decreases due to the viscous-losses. As the flow enters the diffuser, the pressure starts to increase again. It is observed that the numerical and experimental results of pressure coefficient distributions show the same trend. As mentioned earlier, the diffuser was designed to yield an approximately constant adverse pressure gradient, which is confirmed by the linear variation of the pressure in the numerical and experimental results. In addition, as expected the inviscid theory (which the diffuser is designed based on) over-estimates the pressure coefficient along the diffuser upper wall.

Figure 11 shows the predicted secondary flows and the streamwise velocity contours using different turbulence models at section *x*=2082 mm, (i.e. 20 mm before the start of diffuser). As expected only the RSM model is able to predict fairly strong secondary flow patterns. Using alternative vorticity form of the Reynolds-averaged Navier-Stokes equations, one can show that the secondary flows are generated by the axial mean vorticity, which becomes non-zero in a straight duct or pipe only if there are differences between cross-stream normal Reynolds stress ($\overline{v^2} - \overline{w^2}$) or Coriolis forces arising from a spanwise rotation (Speziale *et al.* 1992). Therefore, the linear eddy viscosity turbulence models, based on the Boussinesq hypothesis, are not able to predict secondary flows in a straight non-circular duct. Consequently, the results presented in Fig. 11 are reasonable. Secondary flow vectors in all numerical results seem to have upward directions, which is obviously due to the geometry (the lower wall of diffuser is fixed, while the upper wall is diverging). In addition, the RSM model has predicted two rotating vortices (generated by normal Reynolds stress anisotropy). To understand the structure of these secondary flows it is best to first look at such turbulence driven secondary flows generated in the upstream straight duct. As shown in Fig. 12, with the RSM computations, two counter-rotating vortices are observed in each corner at the section *x*=1500 mm that force the flow to move from the center of the duct to the corner and then back to the center. By moving in the streamwise direction, it is seen that the upper vortices become weaker in section *x*=2632 mm due to the geometry (diverging upper wall). The lower vortex is also merged to the main upward secondary flow forcing the fluid core displacement to the upward direction in a vortical pattern. The streamwise velocity contours in Fig. 13 indicate flatter velocity profiles for $k-\omega$ and v^2-f models.

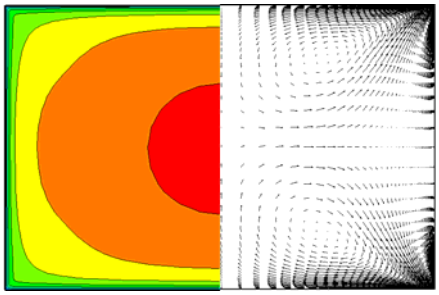

Fig. 12. Vectors of secondary flow (right) and Contours of streamwise velocity (left) in section *x*=1500 m predicted by RSM model.

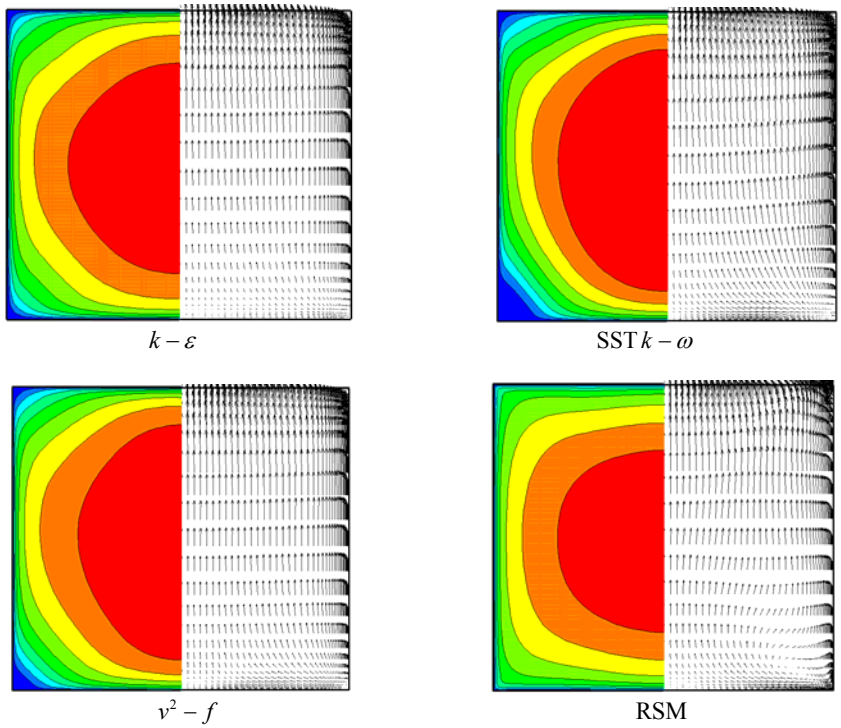

Fig. 13. Vectors of secondary flow (right pictures) and Contours of streamwise velocity (left pictures) in section *x*=2632 m.

The predicted velocity and the turbulence field inside the diffuser using different turbulence models are further presented and compared to the experimental data in the following. These quantities are reported at three different sections of the diffuser symmetry plane. The sections are placed at 2082 (20 mm before the diffuser), 2357 (255 mm into the diffuser) and 2632 mm (530 mm into the diffuser), respectively.

Numerical and experimental profiles of the streamwise component of the velocity are compared in Fig. 14. It is observed that the SST $k-\omega$ model largely over-predicts the velocity field inside the diffuser, which is consistent with the centreline velocity predictions shown in Fig. 9. The other turbulence models demonstrate better streamwise velocity predictions inside the diffuser. As mentioned earlier, the flow entering the diffuser is not fully-developed and thus the significant differences seen in velocity predictions depends on the capability of the turbulence models in reproducing the developing boundary layer in the straight duct. Fig. 14 reveals that among the turbulence models, as expected, the RSM turbulence model returns the best predictions for the streamwise velocity. In addition, a comparison of velocity profiles at the three sections illustrates the rapid boundary layer growth along the diffuser initiated by the trip (i.e. the mean streamwise velocity profile becomes less flat). The streamwise velocity predictions of the RSM model are further compared in log-scale in Fig. 15 in order to investigate the effect of the adverse pressure gradient on the boundary layer development. It is observed that the linear law of the wall, $U^+ = y^+$, holds in the viscous sublayer ($y^+ < 5$) regardless of the adverse pressure gradient. However, with the flow development, the wake region grows both in strength and size. Hence, the outer part of the log region becomes smaller. The increase in the wake component is due to the significant decrease in the skin friction along the diffuser. This feature of adverse pressure gradient on the fluid velocity development has been also reported in the literature (see for example Nagano *et al*., 1993).

The predicted normal velocity profiles inside the diffuser are compared with the measured data in Fig. 16. The normal velocity profiles inside the diffuser are affected by both the diffuser geometry and the secondary flows. Since the first section (*x*=2082 mm) is just before the diffuser, the normal velocity distribution is more affected by the secondary flow motion. However, in the downstream stations the geometry mainly influences the normal velocity profile. As expected, the normal velocities in the first section are lower than those in the downstream stations. As shown earlier the eddy viscosity turbulence models fail to predict correct turbulence driven secondary flows, and as a result they are not able to predict accurate normal velocity profiles in the first section. As expected the RSM model produces a more accurate cross velocity profile in the first station due its ability in prediction of turbulence driven secondary motion as already shown in Fig. 11. In the two downstream sections, the contribution of the geometry on the normal velocity distribution becomes dominant. Hence, the numerical results of different turbulence models are more similar and are closer to the experimental data. Nevertheless,

the results of RSM model are still in superior agreement with the measured data.

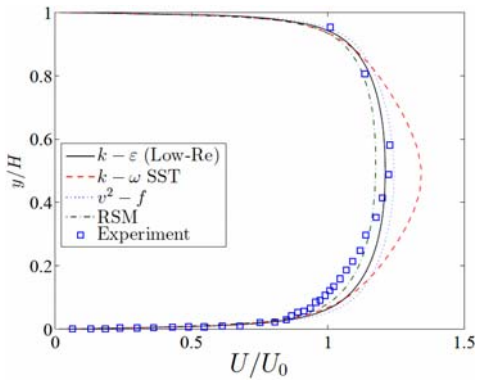

x=2082 mm

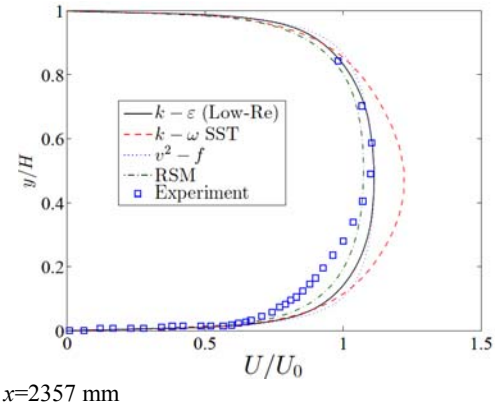

x=2357 mm

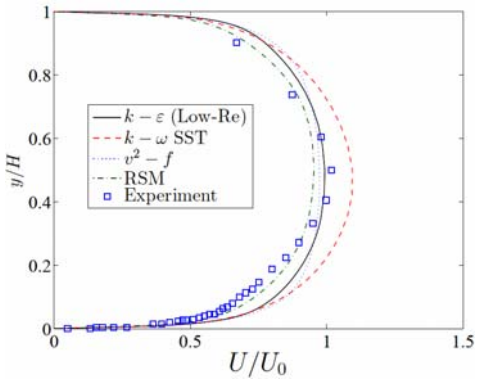

x=2632 mm

Fig. 14. Streamwise velocity along a vertical direction inside the diffuser.

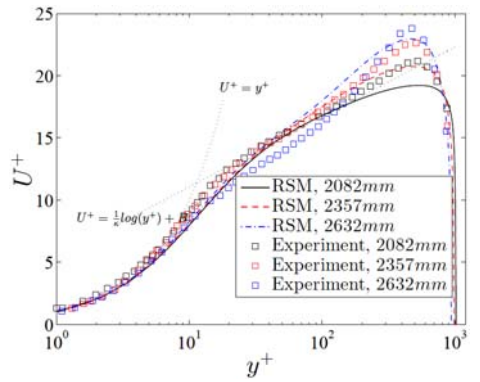

Fig. 15. "Law of the wall" plots of RSM model.

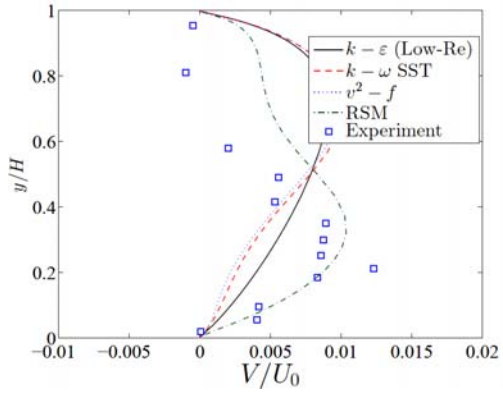

x=2082 mm

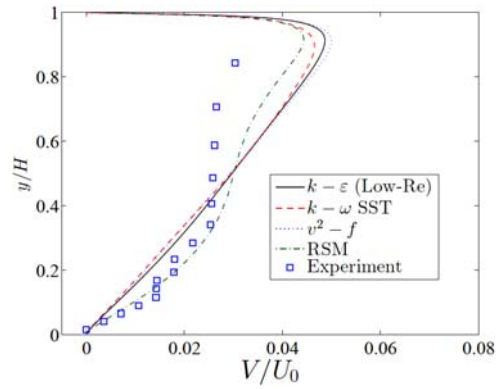

x=2357 mm

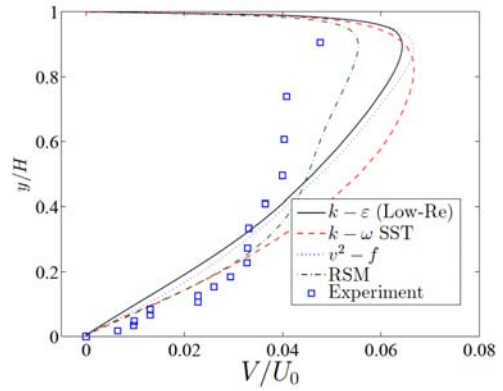

x=2632 mm

Fig. 16. Normal velocity along vertical direction inside the diffuser.

Figure 17 shows comparisons for the streamwise normal Reynolds stress ($\overline{u^2}$) in the diffuser. The comparisons show that the eddy-viscosity based turbulence models, as expected, significantly under-estimate the turbulent normal levels. On the other hand, the RSM model is able to produce accurate predictions for this quantity. The comparison of results in the three sections reveals that the streamwise normal Reynolds stress develops an outer plateau in the presence of an adverse pressure gradient. The intensity of this plateau increases in the streamwise direction. This property of a turbulent boundary layer flow subjected to an adverse pressure gradient is more obvious in a semi-log plot as shown in Fig. 18.

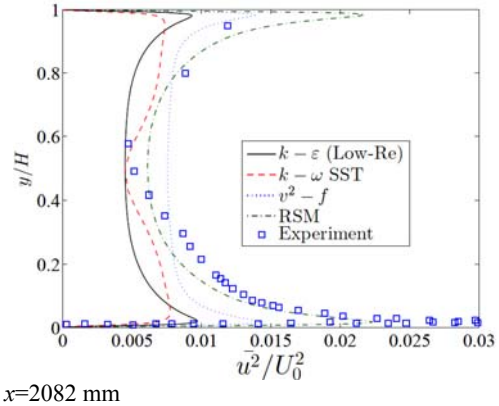

x=2082 mm

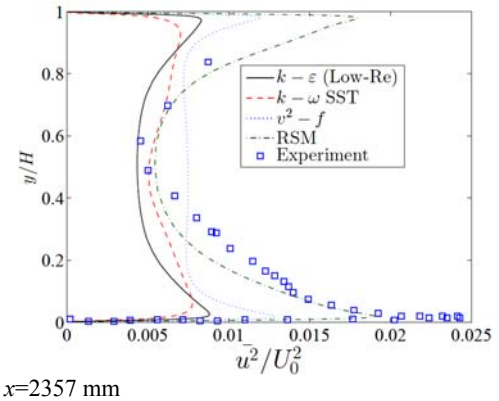

x=2357 mm

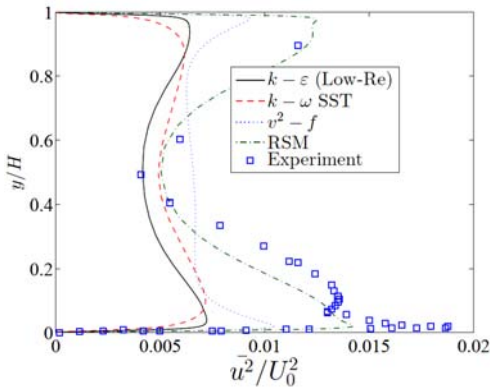

x=2632 mm

Fig. 17. Streamwise component of normal Reynolds stress along vertical direction inside the diffuser.

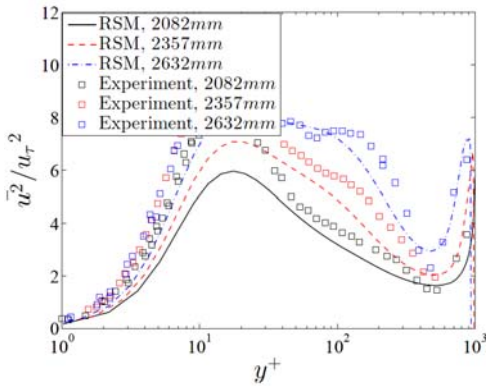

Fig. 18. Streamwise component of the normal Reynolds stress for the RSM model.

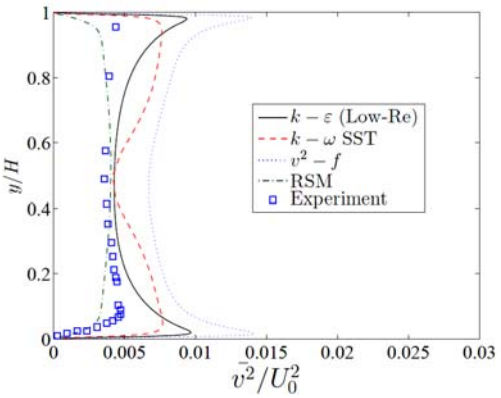

x=2082 mm

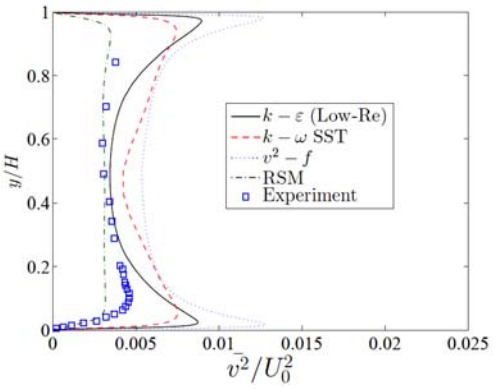

x=2357 mm

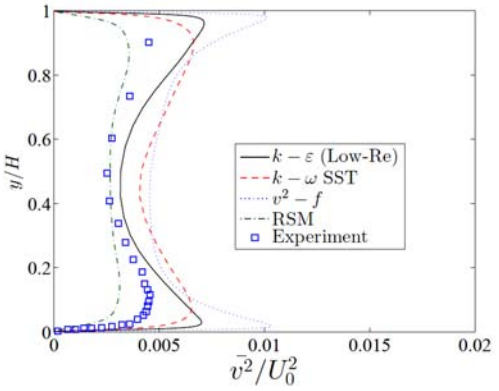

x=2632 mm

Fig. 19. Cross-stream component of normal Reynolds stress inside the diffuser.

Comparisons $\overline{v^2}$ predictions using various turbulence models and experimental data are presented in Fig. 19. As can be observed the all eddy-viscosity based turbulence models over-predict $\overline{v^2}$ levels. As expected, the RSM model returned more reliable $\overline{v^2}$. Numerical and experimental results of shear Reynolds stresses are illustrated in Fig. 20. It is seen that the RSM model is able to produce acceptable results for the turbulent shear Reynolds stress distributions in all three locations. It is noted that the $k-\omega$ and v^2-f models are also yield acceptable results for this quantity.

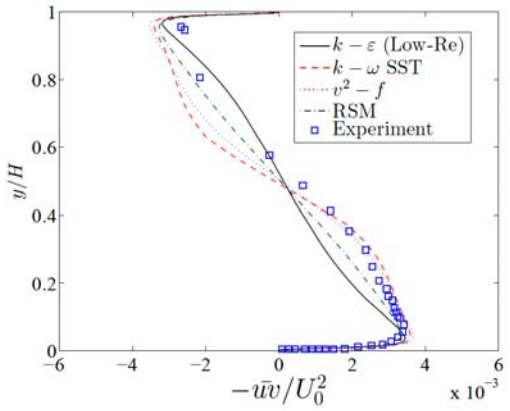

x=2082 mm

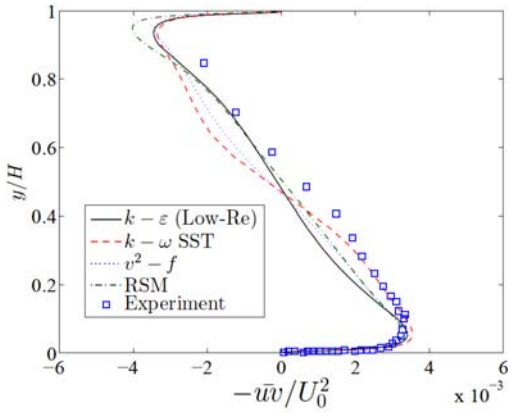

x=2357 mm

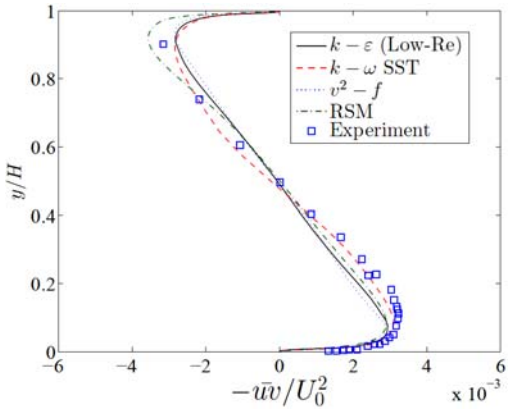

x=2632 mm

Fig. 20. Shear Reynolds stress along vertical direction inside the diffuser.

6. CONCLUSION

The 3D developing turbulent flow through a rectangular asymmetric diffuser with moderate adverse pressure gradient was numerically investigated and the numerical results of the predictions are compared with the LDA data. Such calculations are important in hydraulic machinery flows, due to importance of adverse pressure gradient in these flows. It was observed that the developing flow inside the diffuser is significantly sensitive to the inlet boundary condition. Therefore, the inlet conditions extracted from experimental measurements were employed for the numerical predictions. Four RANS turbulence models are employed for the numerical predictions. The results of centerline velocity in the straight duct demonstrated the best predictions can be obtained using the low-Re $k-\varepsilon$ and RSM turbulence models. The SST $k-\omega$ largely overpredicts the centerline velocity and boundary layer thickness. On the other hand, the RSM model produces most precise results for the pressure recovery. It was observed that the normal velocity distribution inside the diffuser is affected by geometry and secondary flows and the RSM model yields the best predictions for this quantity due to its anisotropy nature. It was further shown that streamwise normal Reynolds stress is significantly underestimated by the isotropic based turbulence models. These turbulence models overpredict the cross-stream normal Reynolds stress. In contrast, the RSM model produces more precise results for the turbulent Reynolds stresses.

ACKNOWLEDGEMENTS

The authors gratefully acknowledge the financial support of Hydraulic Machinery Research Institute of University of Tehran and Swedish Hydropower Centre (www.svc.nu).

REFERENCES

Bradshaw, P. (1967). The turbulence structure of equilibrium boundary layers. *J. Fluid Mech*. 29, 625-645.

Buice, C. U. and J. K. Eaton (1996). Experimental investigation of flow through an asymmetric plane diffuser. *CTR Annual research briefs*-1996, 243-248.

Cervantes, M. J. and T. F. Engström (2008). Pulsating turbulent flow in a straight asymmetric diffuser. *J. Hydraulic Res*., 49 (1), 112-128.

Cherry, E. M., C. J. Elkins and J. K. Eaton (2008). Geometric sensitivity of three-dimensional separated flows. *Int. J. Heat Fluid F*low 29, 803–811.

Cherry, E. M., C. J.Elkins and J. K. Eaton (2009). Pressure measurements in a three-dimensional separated diffuser. *Int. J. Heat Fluid Flow* 30, 1-2.

Chung, D. and D. Pullin (2009). Large-eddy simulation and wall-modeling of turbulent channel flow. Journal of Fluid Mechanics 631, 281–309.

Clauser, F. H. (1954). Turbulent boundary layers in adverse pressure gradients. *J. Aero. Sci*. 21(2), 91–108.

Durbin, P. A. (1995). Separated flow computations with the $k-\varepsilon-v^2$ model. *AIAA Journal* 33 (4), 659-664.

Durst, F., M. Fischer, J. Jovanović and H. Kikura

(1998). Methods to Set Up and Investigate Low Reynolds Number, Fully Developed Turbulent Plane Channel Flows. *J. Fluids Eng.* 120, 496–503.

El-Behery, S. M. and M. H. Hamed (2011). A comparative study of turbulence models performance for separating flow in a planar asymmetric diffuser. *Computers and Fluids* 44, 248–257.

Gibson, M. M. and B. E. Launder (1978). Ground Effects on Pressure Fluctuations in the Atmospheric Boundary Layer. *J. Fluid Mech.* 86. 491–511.

Iaccarino, G. (2001). Prediction of a turbulent separated flow using commercial CFD codes, *J. Fluids Eng*. 123(4), 819-828.

Inouea, M., D. I. Pullina, Z. Harunb and I. Marusicb (2013). LES of the adverse-pressure gradient turbulent boundary layer. *Int. J. Heat and Fluid Flow* 44, 293–300.

Jakirlić, S., G. Kadavelil, M. Kornhaas, M. Schäfer, D. C. Sternel and C. Tropea (2010). Numerical and physical aspects in LES and hybrid LES/RANS of turbulent flow separation in a 3-D diffuser. *Int. J. Heat and Fluid Flow* 31, 820–832.

Jeyapaul, E. (2011). Turbulent flow separation in three-dimensional asymmetric diffusers, PhD Thesis. Iowa State University, United States.

Jones, W. P. and B. E. Launder (1972). The Prediction of Laminarization with a Two Equation Model of Turbulence, *Int. J. Heat and Mass Transfer* 15, 301-314.

Kaltenback, H. J., M. Fatica, R. Mittal, T. S. Lund and P. Moin (1999). Study of the flow in a planar asymmetric diffuser using large eddy simulations. *J Fluid Mech*. 390, 151–185.

Launder, B. E. and B. I. Sharma (1974). Application of the Energy Dissipation Model of Turbulence to the Calculation of Flow near a Spinning Disc, *Letter in Heat Mass Transfer* 1, 131-138.

Lee, J. H. and H. J. Sung (2008). Effects of an adverse pressure gradient on a turbulent boundary layer. *Int. J. Heat and Fluid Flow* 29, 568–578.

Menter, F. R. (1994). Two-Equation Eddy-Viscosity Turbulence Models for Engineering Applications. *AIAA Journal*. 32(8), 1598–1605.

Nagano, Y., M. Tagawa and T. Tsuji (1993). Effects of Adverse Pressure Gradients on Mean Flows and Turbulence Statistics in a Boundary Layer. *Turbulent Shear Flows* 8, 7-21.

Obi, S., K. Aoki and S. Masuda (1993). Experimental and computational study of turbulent separating flow in an asymmetric plane diffuser. *Ninth symposium on turbulent shear flows*, Kyoto, Japan, 305-1–4.

Ohlsson, J., P. Schlatter, P. F. Fischer and D. S. Henningson (2010). Direct numerical simulation of separated flow in a three-dimensional diffuser. *J Fluid Mech*. 650, 307-318.

Rai, S. P. (1986). Wall-wakes in moderate adverse pressure gradients. *J. Hydraulic Res*., 24(5), 377-390.

Schlüter, J. U., X. Wu and H. Pitsch (2005). Large-Eddy Simulations of a Separated Plane Diffuser. *43rd AIAA Aerospace Sciences Meeting and Exhibit*, AIAA 2005-0672.

Speziale, C. G., R. M. C. So and B. A. Younis (1992). On the prediction of turbulent secondary flows, NASA Contractor Report 189722 OpenFOAM 2.0.0 User Guide.